

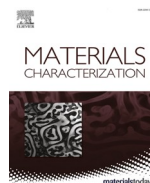


This work was carried out in whole or in part within the framework of the NOMATEN Centre of Excellence, supported from the European Union Horizon 2020 research and innovation programme (Grant Agreement No. 857470) and from the European Regional Development Fund via the Foundation for Polish Science International Research Agenda PLUS programme (Grant No. MAB PLUS/2018/8).

The version of record of this article, first published in *Materials Characterization*, Volume 205, November 2023, 113373, is available online at Publisher's website:

<https://doi.org/10.1016/j.matchar.2023.113373>

This manuscript version is made available under the CC-BY-NC-ND 4.0 license.



# Understanding the role of tetragonal phase in oxidation behaviour of different zirconium-based alloys in air and water vapour conditions – Phase fraction and stress field distribution

Kinga Suchorab<sup>\*</sup>, Magdalena Gawęda, Anna Kosińska, Damian Kalita, Iwona Jóźwik, Łukasz Kurpaska

NOMATEN CoE, NOMATEN MAB, National Centre for Nuclear Research, A. Soltana 7, Otwock-Swierk 05-400, Poland

## ARTICLE INFO

### Keywords:

Raman imaging  
Zirconium oxide  
Phase distribution  
Stress distribution  
Stabilisation factors

## ABSTRACT

The paper investigates the influence of oxidation atmosphere on the corrosion behaviour after 7, 15, and 24 h of different zirconium-based materials, including pure metal, E110, and Zircaloy-2 alloys. The study utilises scanning electron microscopy to perform cross-sectional characterisation. Raman imaging was employed to determine the content and distribution of the tetragonal phase in the oxide scale depending on oxidation parameters. The obtained results were compared with previous thermogravimetric measurements and correlated with stress distribution calculated based on the shift of the selected tetragonal phase band. Additionally, the study reveals a relaxed tetragonal phase in a bulk monoclinic phase. A thorough analysis of Raman spectra allowed correlating spectral features with tetragonal phase stabilisation mechanisms for the tetragonal phase occurring at the metal/oxide interface and in the bulk monoclinic phase.

## 1. Introduction

Zirconium-based alloys are used worldwide for fuel claddings in nuclear reactors, which act as a barrier separating the fuel from the coolant [1]. Prolonged exposure to primary circuit water subjects these alloys to corrosion, which poses a challenge to their operational longevity. In response to this, extensive research has been carried out to gain a deeper understanding of their corrosive behaviour, leading to the development of improved zirconium alloys [1]. Currently, two major zirconium alloys families are distinguished: containing niobium (e.g., E110, M5, Zr-2.65%Nb) or tin (e.g., zircalloys, ZIRLO) [1]. Despite having a comprehensive characterisation of the properties of considered materials, there remains a need for a deeper understanding of the differences of corrosive performance between them, which will lead to better control of the behaviour and, finally, to the further development of zirconium alloys with enhanced corrosion resistance.

The formation of zirconium oxide begins with the simultaneous nucleation of randomly oriented tetragonal and monoclinic grains [1]. Tetragonal phase is known to be metastable at room temperature. However, several factors have been identified to contribute to its stabilisation at room temperature, including high compressive stresses,

oxygen vacancies, cation dopants, and nanoscale grain size [2–4]. The highest influence of the identified stabilising factors was observed on the metal/oxide interface, which corresponds to the highest tetragonal phase fraction. Once the contribution of these factors is no longer sufficient to stabilise tetragonal phase (mainly due to grain growth or stress relaxation), tetragonal grains transform into the stable monoclinic grains [1,3,5]. This transformation is accompanied by volume increase, which can result in the formation of micro-cracks allowing for further oxygen diffusion [6–12]. This leads to further oxidation and this process can be described as a sequential creation of a tetragonal phase at the metal/oxide interface, followed by its transformation into the monoclinic phase [13]. With the progress of oxidation, more and more cracks and porosity are created in the oxide, which ultimately connect with each other, leading to the detachment of parts of the oxide. These effects provide an easy access of the oxidising media to the metal surface, eventually leading to the accelerated corrosion [5,9,12]. This makes it ineffective as a protective layer, that should serve as a diffusion barrier [6].

In the literature [1,14], tetragonal phase has been observed on the metal/oxide interface reaching up to 50% phase fraction. However, the higher tetragonal phase fraction was associated with both protective and

<sup>\*</sup> Corresponding author.

E-mail address: [kinga.suchorab@ncbj.gov.pl](mailto:kinga.suchorab@ncbj.gov.pl) (K. Suchorab).

<https://doi.org/10.1016/j.matchar.2023.113373>

Received 31 July 2023; Received in revised form 25 September 2023; Accepted 4 October 2023

Available online 6 October 2023

1044-5803/© 2023 The Author(s). Published by Elsevier Inc. This is an open access article under the CC BY-NC-ND license (<http://creativecommons.org/licenses/by-nc-nd/4.0/>).

non-protective behaviour [1,7,12,15–17]. Some research [1,5,7] has suggested, that the main impact on the loss of protective behaviour has the amount of tetragonal to monoclinic transformations since it is the main reason of the layer discontinuity. However, the role of tetragonal phase in oxidation progression remains unclear as no specific correlation between tetragonal phase content and tetragonal to monoclinic transitions has been determined [1]. The influence of the tetragonal phase on the oxidation kinetics is of the key importance and for this reason further research on this subject is needed, especially to address some of the remaining questions: what is the most effective approach for enhancing protective properties? Should it be done by increasing the stability of the tetragonal phase, i.e., delay of the transformation, or by completely preventing the creation of the tetragonal phase? Are these mechanisms common for alloys with different compositions? Better understanding of this topic will allow for the further development of zirconium-based alloys and extension of their operational lifetime by enhancing oxidation resistance.

Comprehensive analysis of the oxide formed on zirconium-based materials can be achieved through Raman imaging. This technique is susceptible to even minor structural changes in the examined material and allows for precise differentiation of oxide polymorphs, as their Raman spectra differ [14]. The factors stabilising the tetragonal phase impact the observed Raman spectra by affecting the position, width, and intensity of Raman bands [2]. Moreover, previous comparative research between Raman spectroscopy and X-ray diffraction has demonstrated applicability of Raman spectroscopy for calculating the tetragonal phase content and stress distribution within the examined oxide [18,19]. However, so far, stress has mostly been determined based on single spectral points measurements [3,18,20–24], and data providing detailed information on its spatial distribution in the material, for example by applying Raman imaging, are rather laconic [5,11,12,14,15,25]. Moreover, there is still a need to define a correlation between the content and distribution of the tetragonal phase and the corresponding structural changes. Identifying and understanding the stabilisation mechanisms are crucial steps toward the further advancement of zirconium alloys.

In the present work, Raman imaging was employed to monitor the distribution of the tetragonal phase after oxidation under varying conditions: time and atmosphere. Samples of zirconium and its different alloys were evaluated in terms of their oxidation performance. Particular attention was given to the influence of the oxidation atmosphere on the formation of the tetragonal phase and accompanying spectral changes. The analysis of variations of the Raman parameters allowed correlating the presence of the tetragonal phase with the oxidative behaviour and stress distribution. Based on obtained data, its role in the oxidation process and cracks formation was analysed, considering occupied oxide area and corresponding stress gradient. Despite that, different mechanisms of tetragonal phase stabilisation were described and correlated with tetragonal phase location.

## 2. Materials and methods

### 2.1. Material preparation

In our research, pure zirconium (Goodfellow), as well as the commercial alloys E110, and Zircaloy-2, were utilised. Zirconium was chosen for this study as a reference material, while E110 and Zircaloy-2 were selected due to their application in nuclear reactors, containing niobium or tin respectively. Pure zirconium and Zircaloy-2 were in the

form of thin foils (0.5 mm), whereas E110 was in the form of fuel cladding rods, that were cold rolled to match the shape of the other materials. The composition of the commercial alloys were verified using scanning electron microscopy (SEM) with energy-dispersive X-ray spectroscopy (EDS), and the results were found to be consistent with the compositions reported in the literature [1,14]. The compositions of these materials, as well as the composition of pure zirconium provided by Goodfellow, are presented in Table 1.

All samples were cut into 10x10x0.5 mm pieces using the CUT E 350 EDM machine (AgieCharmilles), which provides a cutting precision of 0.1 mm. Subsequently, the samples were annealed for 1 h at 600 °C, following the approach from the literature [26,27]. This procedure is known to be sufficient to achieve a fully recrystallized microstructure, eliminating any effects originating from the fabrication process. After initial thermal treatment, samples were prepared for the isothermal oxidation process by grinding with SiC paper up to grade 4000× and polishing with colloidal alumina solution to obtain a mirror-like surface. Manual grinding and polishing were performed using QATM Qpol 250 M2. Isothermal oxidation processes were carried out in Czylok tube furnace PRC 110 M/GWP equipped with a steam generator. The furnace reactor tube is divided into two zones: a working chamber and a heater for the process gas mixture with steam. Oxidation experiments were conducted using either air or water steam atmospheres at 600 °C for durations of 7, 15, or 24 h. The mass flow rate of water produced, dispensed by a pump into the steam generator, was set at 50 g/h. Temperature and humidity in the laboratory were controlled and during the experiments they were, respectively, 22 °C and 45%. All tests were performed under these consistent laboratory conditions. The presented oxidation conditions represent the transient conditions that may occur within the reactor, specifically those involving a sudden increase in temperature. Moreover, these conditions accelerate the oxidation process, thus enabling the comparison of multiple specimens over a shorter period. While examining transient oxidation conditions in a reactor, the existed pre-oxidation layer should be considered. However, previous studies have shown [28,29], that its effect on oxidation kinetics is only moderate up to 700 °C and significant after elongated thermal treatment (80 h). Consequently, the impact of the existing pre-oxidation layer was neglected and will not be considered in this article, particularly within the relatively short time period employed in this experiment. Afterward, samples were mounted in an epoxy resin to allow cross-section observations. For this purpose, a mounting press QATM OPAL 410 was used. Finally, the resin-embedded samples were slightly polished to remove resin contamination from the examined surface without damaging the oxides. However, it should be noted, that the proposed sample preparation procedure by Godlewski, may lead to some degree of stress relaxation. As a result, all the measurements performed should be considered semi-quantitative rather than fully quantitative [30].

### 2.2. SEM

The microstructural cross-section observations of zirconium oxides were carried out using scanning electron microscope Thermo Fisher Helios 5UX, equipped with an advanced in-lens detection system and concentric back-scattered detector (CBS). The images were collected at the acceleration voltage of 10 kV.

**Table 1**  
Zirconium and zirconium alloys compositions [1,14].

Material	Sn	Fe	Cr	Nb	Ni	C	Hf	O	N	H
Zr [ppm]	–	200	200	–	–	250	2500	1000	100	10
E110 [wt%]	–	–	–	1.0	–	–	–	–	–	–
Zircaloy-2 [wt%]	1.5	0.14	0.1	–	0.06	–	–	–	–	–

### 2.3. Raman imaging

The technique used for structural analysis the oxide cross-section was Raman imaging with a WITec alpha 300R microspectrometer, utilising a 532 nm laser line, a 100× Zeiss LD EC Epiplan-Neofluar lens (NA = 0.9), a 1800 lines/mm grating, and a CCD detector. The utilised measurement setup provided a spatial resolution of 361 nm. Every measurement was taken with an integration time of 5 s. The laser power was set to 10 mW to achieve a desirable signal-to-noise ratio. The selected laser power was tested on the samples prior to the experiments to ensure that it does not induce any structural changes and does not lead to excessive heating and phase transition. It is important to note that previous research has indicated that the influence of the laser power on the shift of Raman bands is relatively small compared to the influence of the strain [31]. Furthermore, all measurements were performed using the same laser power, ensuring a comparable influence on the calculated stress. For proper imaging of the interphase, which is about several hundred of nanometers thick, and to detect any subtle changes, a constant step size of 0.1  $\mu\text{m}$ , which was possible due to a piezo stage built into the spectrometer, was chosen. The map size was adjusted to match the oxide thickness. They ranged from 3 to 6  $\mu\text{m}$  in height and from 10 to 25  $\mu\text{m}$  in width. The WITec Control FIVE 5.2 PLUS software was utilised to gather Raman data. The initial analysis included baseline correction and cosmic-ray removal (the CRR filter). A linear function was used to correct the baseline for Zr and E110 samples, while a quartic function was needed for the elevated background in the low Raman shift range of Zircaloy-2 samples. Whenever this procedure did not provide satisfactory results, the spectrum range was narrowed down to the bands of interest to facilitate background removal. All cross-sectional measurements were performed at a significant distance from the edges, where the oxide thickness was recognised to be constant (it is typical to be thicker at the edges). This allowed to mitigate edge effects, which is accelerated corrosion process occurring at the edges of flat samples, as observed by several authors [25,32].

### 2.4. Raman data analysis

Obtained Raman data were then analysed in terms of band intensity, band positions, and full width at half maximum (FWHM). Previous studies have shown that it is possible to estimate the tetragonal phase volume fraction based on the band intensity ratio. The relationship (1) was established by Godlewski [18]:

$$\%_{\text{tetragonal}} = \frac{Int_{T1}}{Int_{M1} + Int_{M2} + Int_{T1}} \quad (1)$$

Where  $Int_{(x)}$  stands for maximum intensity of particular monoclinic ( $M1 \approx 175 \text{ cm}^{-1}$ ;  $M2 \approx 185 \text{ cm}^{-1}$ ) and tetragonal ( $T1 \approx 285 \text{ cm}^{-1}$ ) bands. To determine the tetragonal phase distribution within the oxide scale, the Raman spectra from every map were divided with K-Means Cluster analysis (KMC) into regions based on differences in relative intensity of tetragonal band T1 as described elsewhere [33]. The particular cluster spectra were fitted to extract band parameters. Obtained bands positions were assigned to corresponding Raman modes (Fig. 1) according to the literature [19,34]. Intensity values were applied to Eq. (1) and allowed estimating tetragonal phase percentage content in particular clusters. It is important to point out, that several factors (such as texture) can influence the intensities of zirconia bands. However previous research have shown, that it does not significantly alter the phase proportion calculations since they depend on relative intensity of multiple bands [19].

Distributions of full width at high maximum (FWHM) and band shift from the initial position were obtained by applying the fitting function built in the WITec environment. FWHM fluctuations provide an evidence of structure distortion, as has been shown in previous studies [14,35]. On the other hand, based on the shift from the initial band position, it is possible to determine the stress field in the examined material using Eq. (2) [19]:

$$\sigma = \Delta\theta / \pi \quad (2)$$

Where  $\sigma$  is stress expressed in GPa,  $\pi$  is a piezo-spectroscopic constant expressed in  $\text{cm}^{-1} \cdot \text{GPa}^{-1}$ , and  $\Delta\theta$  is the Raman shift difference expressed in  $\text{cm}^{-1}$  (Eq. (3)) for a given band positions between stressed  $\Delta\theta(T, \sigma)$ , and unstressed  $\Delta\theta(T, 0)$  samples [36].

$$\Delta\theta = \Delta\theta(T, \sigma) - \Delta\theta(T, 0) \quad (3)$$

The band position for monoclinic bands can be determined using the calibration described in [37]. Since the tetragonal phase is unstable at room temperature, obtaining a stress-free sample was not feasible. Thus, following the approach in the literature [38], the maximal observed Raman shift was determined as the unstressed tetragonal Raman shift individually for every material, considering that no tensile stresses are expected in the oxide (as the lattice mismatch between Zr and  $\text{ZrO}_2$  results in compressive stresses).

However, it is important to note that previous studies have demonstrated [39,40], that the Raman shift is influenced not only by residual

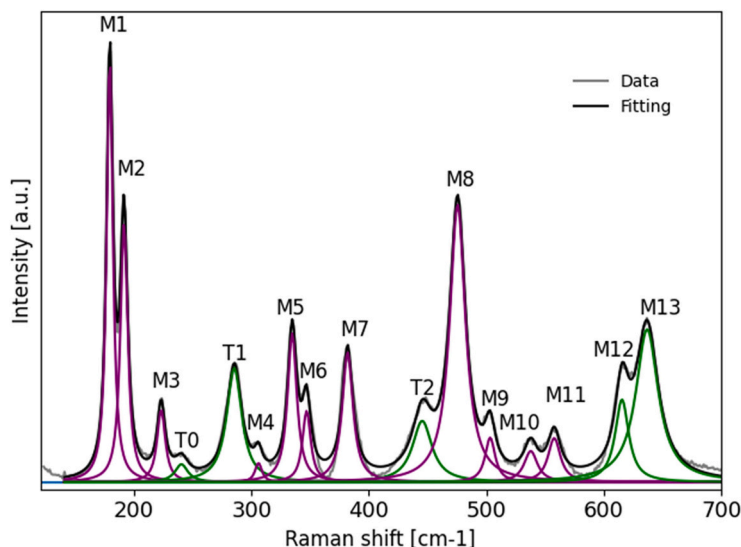


Fig. 1. Distinctive fitted Raman spectrum of zirconium oxide with modes assignment and applied fitting ranges [19,34].

Band assignment	Raman modes	Raman shift [cm <sup>-1</sup> ]	Fitting range [cm <sup>-1</sup> ]
M1	A <sub>g</sub> + B <sub>g</sub>	179	170 - 190
M2	A <sub>g</sub>	191	180 - 200
M3	B <sub>g</sub>	223	215 - 225
T0	E <sub>g</sub>	240	235 - 237
T1	E <sub>g</sub>	285	280 - 290
M4	A <sub>g</sub>	306	305 - 307
M5	B <sub>g</sub>	335	310 - 340
M6	A <sub>g</sub>	347	335 - 355
M7	B <sub>g</sub>	382	380 - 400
T2	E <sub>g</sub>	445	440 - 450
M8	A <sub>g</sub>	475	465 - 480
M9	B <sub>g</sub>	503	495 - 510
M10	B <sub>g</sub>	538	530 - 550
M11	A <sub>g</sub>	558	550 - 570
M12	B <sub>g</sub>	615	610 - 625
M13	E <sub>g</sub>	637	630 - 650

stress but also by the size of grains. The growth of grains at elevated temperature results in Raman position shifts toward lower values (below  $4 \text{ cm}^{-1}$ ) [41]. The influence on the Raman shift is opposite to the changes in compressive stress, as the grain size is expected to increase with the distance from the interface while the compressive stress is decreases. While the proposed equation remains valid, it does not differentiate the individual contributions of those two factors. As a result, it should be acknowledged that the obtained stress values may be slightly underestimated. Still, this equation provides valid representation of stress state in the material.

Piezo-spectroscopic constants determined by Bouvier represent the hydrostatic stress state in the oxide [19]. Nevertheless, the stresses that arise during oxide growth are generally assumed to be equi-biaxial [3,19]. Since Raman measurements are performed on the sample surface and stress perpendicular to the surface is not considered, they have also been locally treated as uniaxial in the literature [35,42]. Therefore, assuming that the material is isotropic, stresses can be easily recalculated from hydrostatic to uniaxial or biaxial, using typical relationship from classical mechanic, as presented in Eq. (4) [43]. Additionally, Limarga [44] has validated this approach for zirconium oxide, demonstrating that the piezo-spectroscopic constant obtained via loading with a uniaxial compression is consistent with that obtained through hydrostatic pressure. Based on that, the hydrostatic piezo-spectroscopic constant obtained by Bouvier can be recalculated to uniaxial or biaxial (Eq. (5)) and applied to Eq. (2).

$$\sigma_{\text{hydrostatic}} = \frac{2}{3}\sigma_{\text{biaxial}} = \frac{1}{3}\sigma_{\text{uniaxial}} \quad (4)$$

$$\pi_{\text{uniaxial}} = \frac{1}{2}\pi_{\text{biaxial}} = \frac{1}{3}\pi_{\text{hydrostatic}} \quad (5)$$

Piezo-spectroscopic uniaxial constant values for chosen bands are shown in Table 2.

### 3. Results and discussion

#### 3.1. Thermogravimetric analysis

Oxidation of zirconium alloys takes place following various oxidation kinetics (for example cubic, parabolic, sub-parabolic or linear) depending on the alloy composition, oxidation conditions and the stage of the process. In general, the more linear oxidation rate is, the faster the process occurs and worsens the alloy resistance to oxidation. The exemplary weight gain profiles for various zirconium-based alloys in air and water steam are presented in Fig. 2 and Fig. 3, respectively.

Thermogravimetric measurements of Zr, E110, and Zircaloy-2 are presented in Fig. 2 as a summary of previous research [32,45]. These materials were subjected to isothermal oxidation under conditions that closely resemble those employed in our experiments (600 °C, air atmosphere, 20 h). The presented results indicate that, under these oxidation conditions, pure zirconium experiences the slowest mass gain among examined materials. Moreover, no sign of breakaway was observed. Therefore, it can be concluded that pure zirconium exhibits superior oxidation resistance compared to the other examined materials. At the beginning of the process, E110 and Zircaloy-2 have similar oxidation rates. However, on the oxidation kinetic curve of Zircaloy-2, a kinetic transition can be observed after 9 h, and the change of oxidation rate from sub-parabolic to linear follows that. In contrast, pure Zr and E110 remain in a pre-transition regime for the 20-h oxidation process. Since the Zircaloy-2 is the only examined alloy that experiences

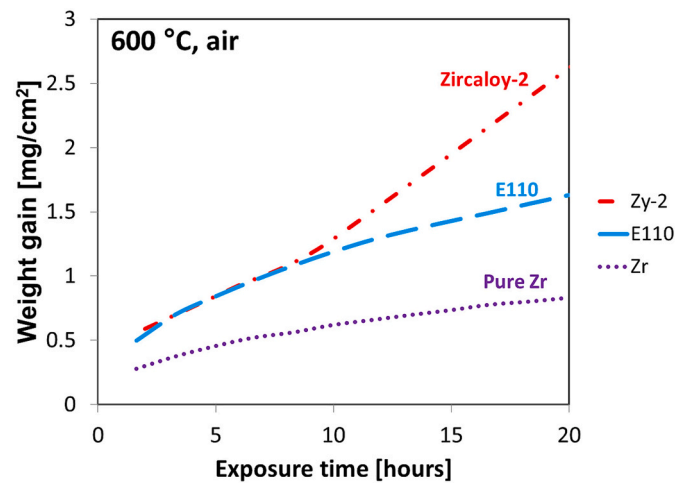


Fig. 2. Isothermal mass gain profiles versus oxidation time for pure Zr, E110, and Zircaloy-2 in an air atmosphere at 600 °C (based on previous studies [32,45]).

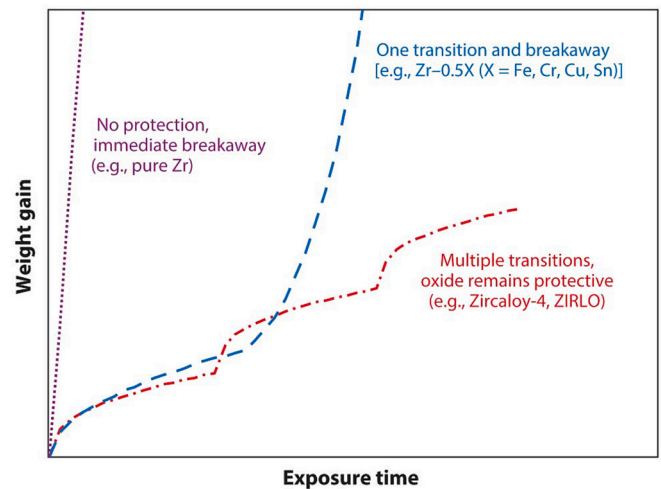


Fig. 3. The schematic kinetic curves for zirconium-based alloys oxidised in water steam [1]

breakaway, which results in a significant oxidation acceleration, it suggests that in applied measurement conditions, it demonstrates inferior oxidation performance compared to other alloys.

As of the current date, there is a lack of experimental data related to the behaviour of these materials during oxidation in water steam at 600 °C for 24 h. Nevertheless, the behaviour of the analysed materials in water steam has been characterised in previous studies under alternate conditions (at 360 °C and 500 °C) [46]. Based on these research, a schematic kinetic curves for different types of zirconium alloys have been created and presented in Fig. 3 [1]. In a water steam atmosphere, the oxidation behaviour of pure zirconium changes drastically, with the immediate occurrence of breakaway [46]. In contrast, alloys do not demonstrate a similar correlation between the oxidation rate and the oxidation atmosphere. Therefore, it can be assumed that alloys provide better oxidation resistance in water steam than pure zirconium, as no immediate breakaway was observed [1].

#### 3.2. Oxide cross-section characterisation

The microscopic observation of the cross-section was used to measure the oxide thickness of each sample. The average values with error bars, obtained from measurements at 10 different locations across the

Table 2

Values of uniaxial piezo-spectroscopic constant for T1 band [19,44].

Band	$\pi_{\text{uniaxial}} [\text{cm}^{-1} \cdot \text{GPa}^{-1}]$	$\pi_{\text{biaxial}} [\text{cm}^{-1} \cdot \text{GPa}^{-1}]$	$\pi_{\text{hydrostatic}} [\text{cm}^{-1} \cdot \text{GPa}^{-1}]$
T1	1.2	2.4	3.59



oxide, are shown in Fig. 4. The data presents a correlation between the increase in the oxide layer thickness and the prolonged duration of the oxidation process. The growth of oxide thickness observed in samples oxidised in the air (Fig. 4 (a)) is generally consistent with the results obtained from thermogravimetric analysis presented in Fig. 2. Among the materials examined, pure zirconium exhibited the lowest oxide thickness after 7 and 15 h, indicating the slowest oxidation rate. After 24 h, the oxide thickness of pure zirconium was higher than expected based on TGA results (Fig. 2). This divergence could be attributed to differences between the oxidation atmospheres used in the TGA and furnace oxidation. While TGA measurements were performed in synthetic air with a constant flow, oxidation in the furnace was performed in ambient air without forced gas flow. Nevertheless, the oxide layer formed on pure zirconium after 24 h of oxidation in the air atmosphere was found to be continuous and consistent along the surface. As a result, pure zirconium exhibited excellent corrosion resistance in the air atmosphere. E110 and Zircaloy-2 reached comparable oxide thicknesses, except for the E110 sample oxidised for 24 h, where the thickness was found to be reduced. This deviation may be attributed to systematic oxide detachment along the surface rather than being a deviation from the established relationship between oxidation duration and oxide thickness. According to the TGA results Fig. 2, Zircaloy-2 was expected to have a significantly larger oxide thickness than E110 after 15 h of oxidation in the air. However, the experimental results showed similar oxide thickness for both materials, suggesting more minor differences in oxidation kinetics between these alloys than were presented by TGA results. Considering the time elapsed between the TGA experiments carried out on both materials, this discrepancy may be due to the differing accuracy of the equipment used.

In the case of oxidation in water steam (Fig. 4 (b)), a significant change in the oxide thickness of pure zirconium was observed. The considerable thickness of the oxide was increased in this material oxidised for 7 h, indicating a very rapid oxidation rate and a breakaway event. This outcome contrasts with the oxidation in the air atmosphere and is consistent with previously reported observations of zirconium in water steam [1]. Further measurements on samples oxidised for extended durations revealed a decrease in the oxide thickness, likely caused by the detachment of the oxide. Furthermore, a substantial increase in the oxide thickness of E110 occurs only after 24 h, and no significant differences in oxide thickness on examined samples of Zircaloy-2 oxidised in two atmospheres were observed.

To further investigate evolution of oxide thickness, cross-sectional SEM observations were performed on samples subjected to oxidation in both air and water steam at 600 °C for 24 h. The results for the specific alloys are presented in the Fig. 5 (a-f). The observed oxide microstructure demonstrates correlation with oxide thickness and provides an explanation of the underlying mechanism driving oxide detachment. The SEM observations revealed the presence of porosity and cracks

parallel to the surface, both of which are characteristic features of non-protective zirconium oxide. According to the literature [13], cracks can interconnect, resulting in a loss of adhesion within the oxide layer. Consequently, this loss of adhesion leads to the delamination of a part of the oxide, leaving solely a thin adhesive oxide at the interface. This phenomenon is captured in Fig. 5 (d), where an interlinked network of cracks disrupts the central part of the oxide layer, causing two distinct segments of the oxide to become disconnected. This strongly suggests that the oxide may have initially possessed a much greater thickness, but due to its inconsistent nature, a substantial portion of the oxide delaminated. This explains the significant reduction in oxide thickness observed in the case of E110 subjected to 24 h oxidation in an air environment (Fig. 4 (a)). A similar phenomenon is observed for pure zirconium oxidised in water steam for the same duration (Fig. 5 (b)), resulting in an irregular oxide surface observed, and the detachment of portions of oxide due to interconnected cracks. These findings, encompassing oxide thickness and the microstructural cross-sectional characterisation of oxide, point to an advanced stage of corrosion for these materials. Moreover, the presence of these irregularities in the oxide, such as the oxide delamination, cracks, and porosity, contributes to the acceleration of the oxidation process by facilitating direct contact between the oxidation medium and the metal.

In contrast, other samples displayed no signs of oxide delamination. Although, parallel cracks are present within the oxide structure, they remain isolated, promoting better consistency and adhesion within the oxide layer. This observation indicates better corrosion resistance exhibited by these samples. Consequently, it can be concluded that zirconium demonstrated enhanced oxidation resistance in air compared to water steam, whereas E110 presents the opposite behaviour. These findings are consistent with TGA data known from the literature (Fig. 2 and Fig. 3). In the case of Zircaloy-2, the created oxide showed similarities regardless of the oxidation atmosphere.

### 3.3. Raman analysis of interface oxide

Raman imaging was employed for cross-sectional observation of the oxide to characterise it in terms of phase content and distribution. Based on T1 band intensity differences, spectra were divided into clusters presenting the phase distribution. Average cluster spectra were fitted, and intensities of M1, M2, and T1 bands were applied to Eq. (1). This allowed estimation of the tetragonal phase content in particular clusters presented as a scale with the corresponding colour. Additionally, T1 band shift from the initial position was used to Eq. (2) to determine stress distribution through the oxide. Results of this analysis are presented in Figs. 6, 7, and 8.

For all the examined materials, a predominantly tetragonal phase is present on the metal/oxide interface, and its content decreases with the distance from the interface. Tetragonal phase thickness is highly

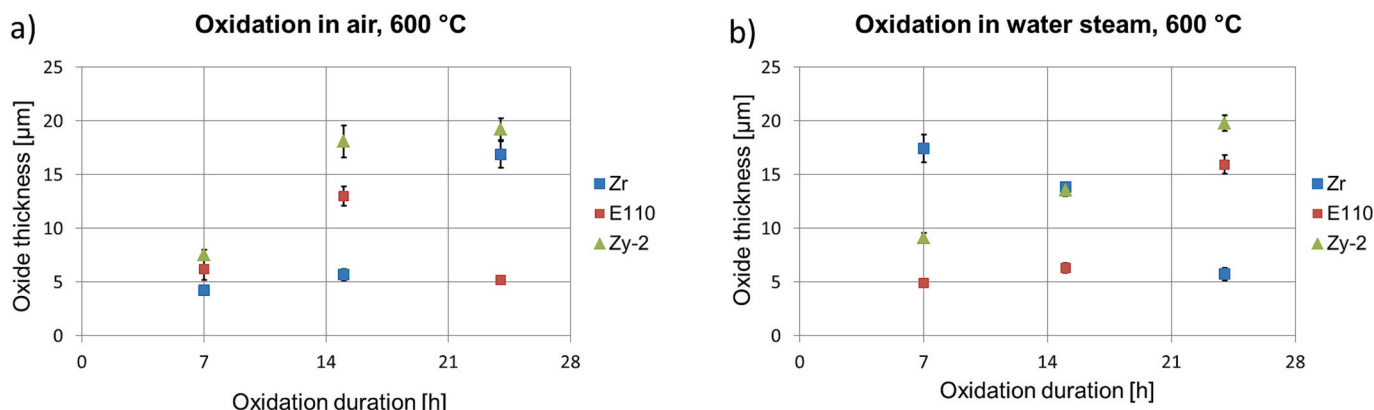
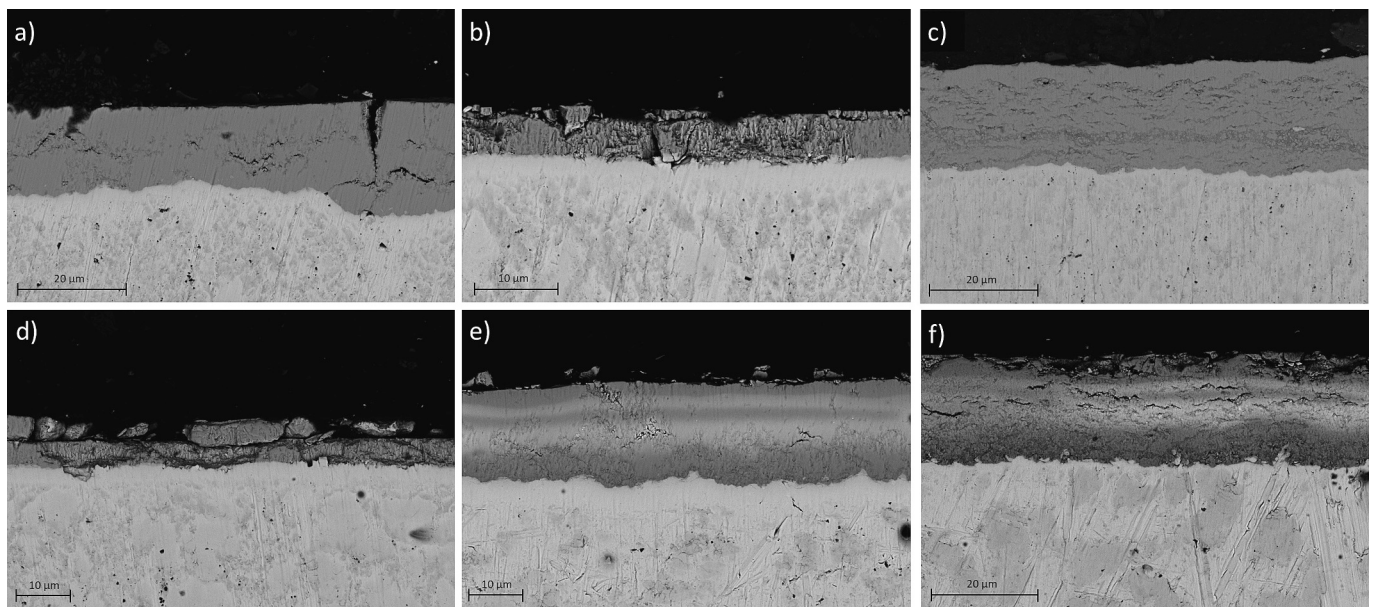
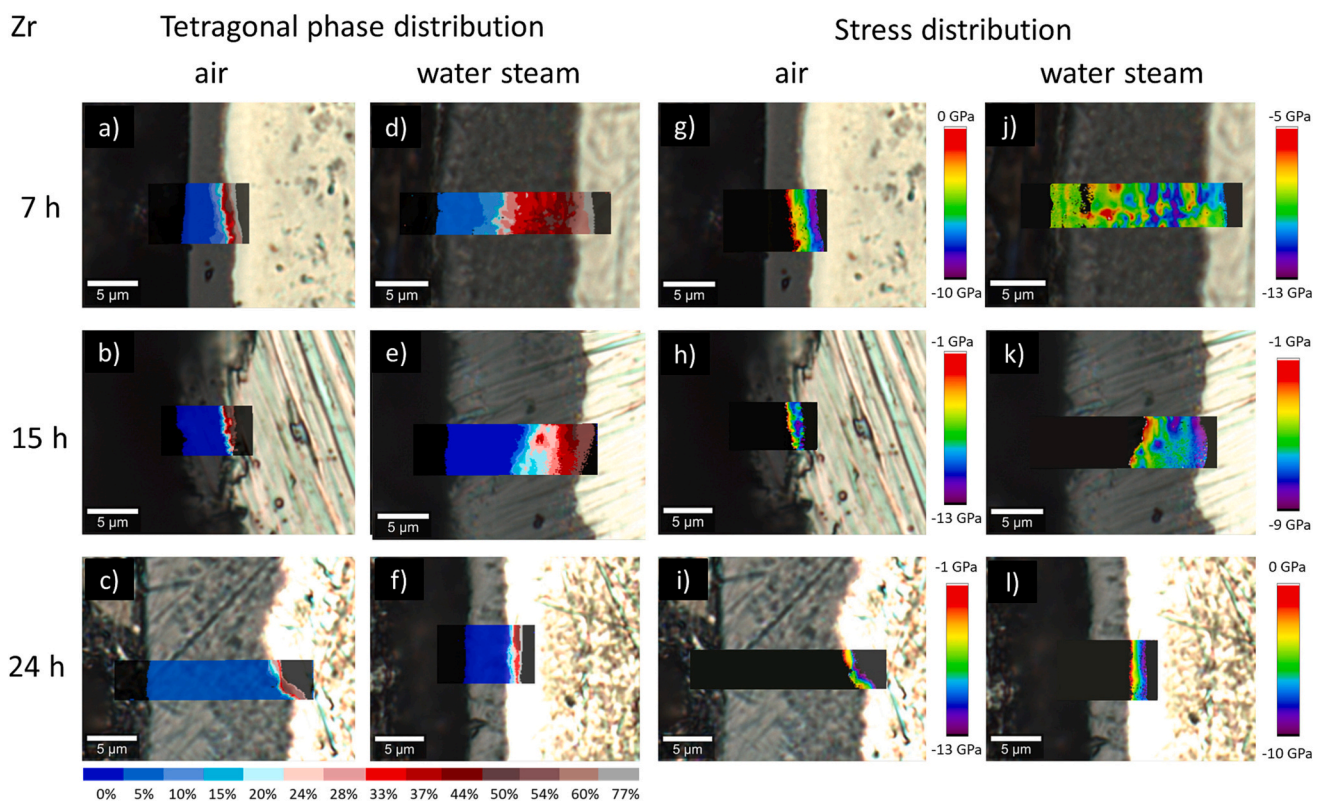


Fig. 4. Measured oxide thickness of Zr, E110, and Zircaloy-2 oxidised at 600 °C in: a) air; b) water steam.



**Fig. 5.** SEM images of metal-oxide interface developed during oxidation in air at 600 °C for 24 h on the: a) pure zirconium; b) E110; c) Zircaloy-2; and in water steam at 600 °C for 24 h on the: d) pure zirconium; e) E110; f) Zircaloy-2



**Fig. 6.** Raman imaging results for pure zirconium oxidised at 600 °C: (a-f) tetragonal phase content and distribution; (g-l) stress distribution calculated based on T1 band shift from assumed stress-free position.

dependent on oxidation parameters.

The thicker tetragonal phase appears at the beginning of the oxidation process, and its amount decreases with the oxidation time, whereas the oxide thickness increases. Therefore, along with oxidation time, the monoclinic phase becomes predominant in the oxide. A small volume fraction of tetragonal phase goes together with parallel cracks created through phase transformations. The cracks can eventually connect,

leading to loss of oxide consistency and delamination.

Furthermore, tetragonal phase content and distribution are related to the stress level and distribution in the oxide. Generally speaking, the highest compressive stress in the oxide occurs on the metal/oxide interface, where the tetragonal phase content is the largest. Then, following the tetragonal phase changes, compressive stress decreases with the increasing distance from the interface. The noticed correlation



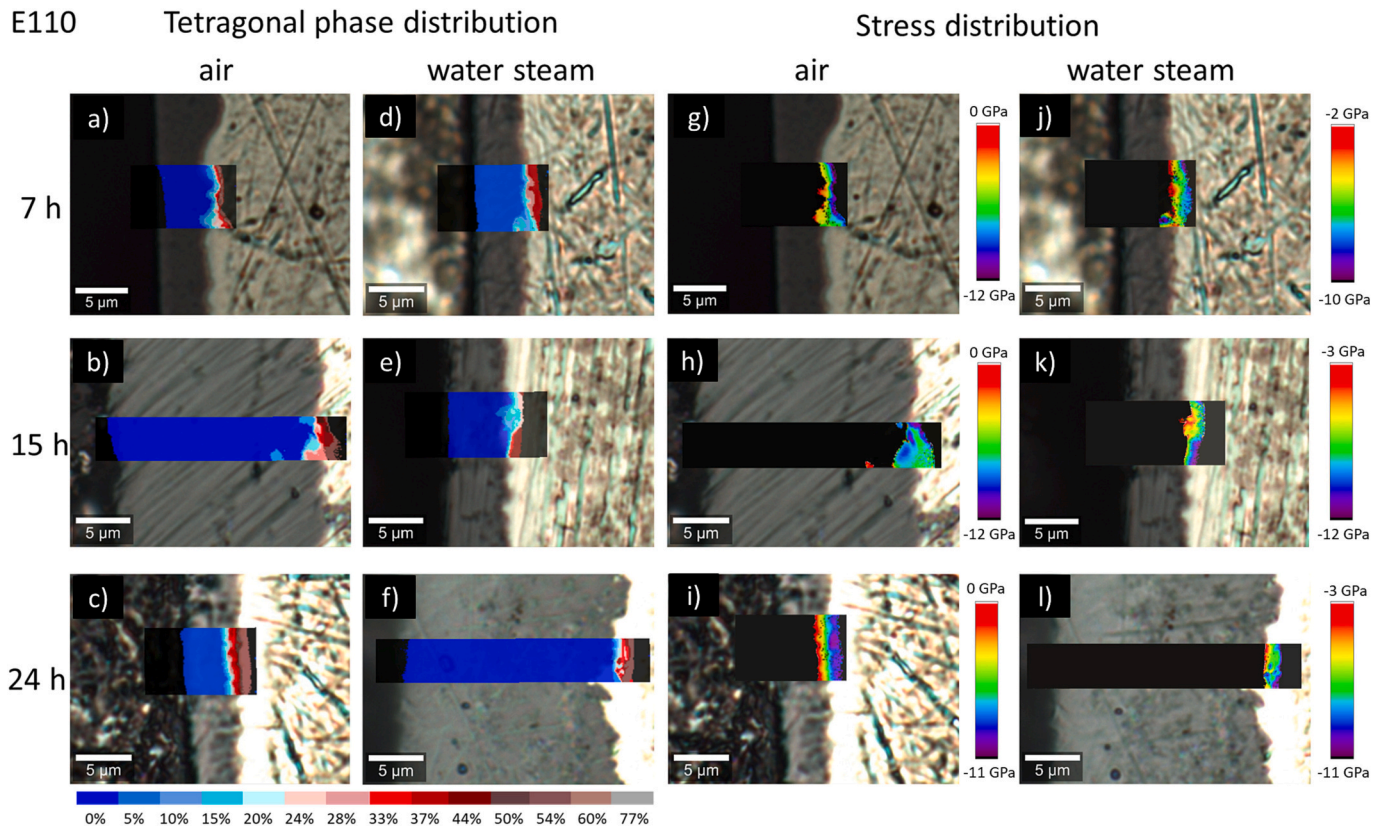


**Fig. 7.** Raman imaging results for E110 oxidised at 600 °C: (a-f) tetragonal phase content and distribution; (g-l) stress distribution calculated based on T1 band shift from assumed stress-free position.

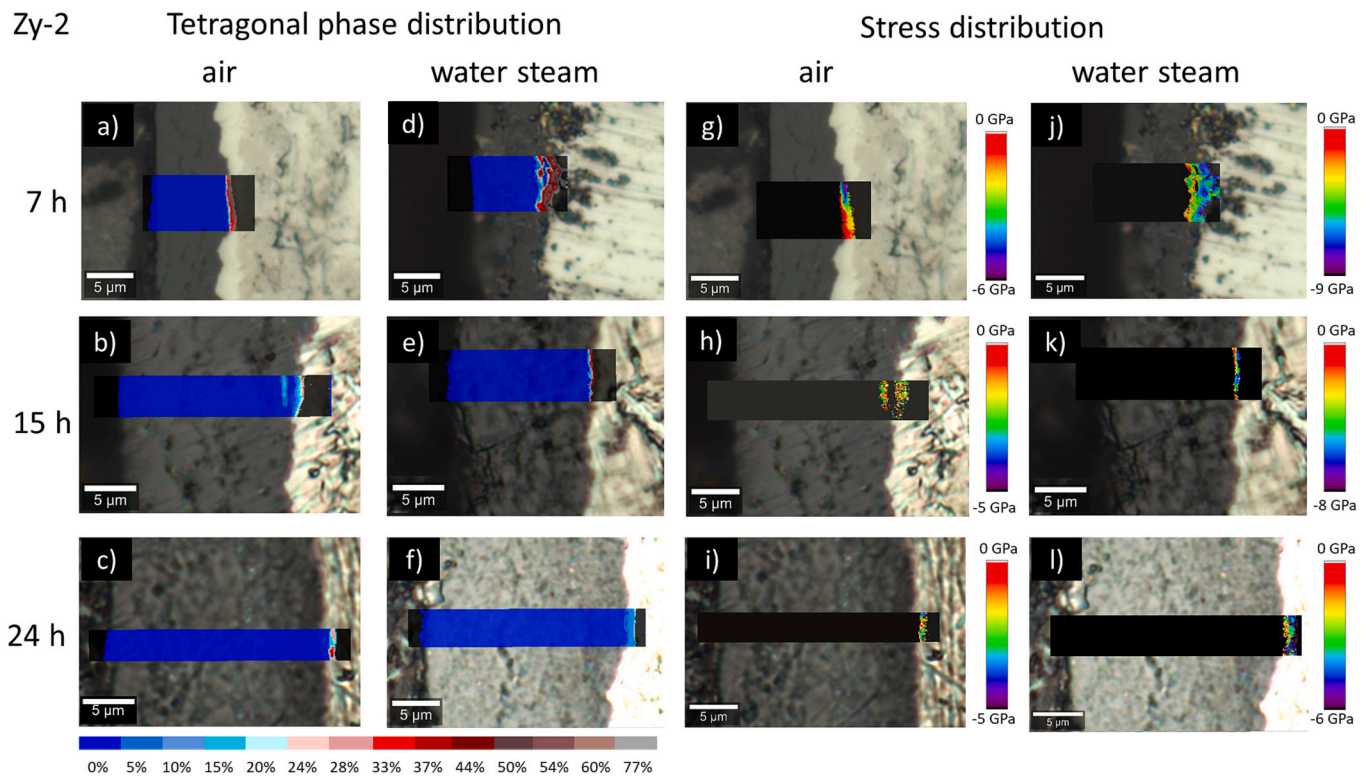


**Fig. 8.** Raman imaging results for Zircaloy-2 oxidised at 600 °C: (a-f) tetragonal phase content and distribution; (g-l) stress distribution calculated based on T1 band shift from assumed stress-free position.



provides evidence that the tetragonal phase at the metal/oxide interface is stabilised mainly by compressive stress, whereas the transformation is accompanied by stress relaxation. This abrupt change in stress level may be responsible for oxide cracking. It is important to note that this correlation may vary depending on the material under examination and the used oxidation parameters.

### 3.4. Pure zirconium

As it was already mentioned, the atmosphere may have a significant influence on oxidation kinetics. In the case of pure zirconium, water steam significantly enhances oxidation, which is presented in Fig. 6 (d-f) in comparison to (a-c). A noticeable difference in oxide thickness is seen already after 7 h. The accelerated corrosion process resulted in faster oxide growth, and suddenly the tetragonal phase is present throughout the entire oxide, contributing to the monoclinic phase with different content (Fig. 6 (d)). This reveals that the oxide growth was rapid enough to prevent the transition from the tetragonal to the monoclinic phase. Moreover, an increase in oxidation time (Fig. 6 (e-f)) led to a decrease in the amount of tetragonal phase present throughout the oxide layer. This implies that the tetragonal phase transforms rapidly into a monoclinic phase across the entire oxide. This is the opposite phenomenon to the corrosion in ambient air (Fig. 6 (a-c)), where transformations gradually occur with the oxide growth. This indicates, that a large amount of unstable tetragonal product was obtained through the oxide, that rapidly transforms into monoclinic phase.

Stress field analysis demonstrated that the highest stress was observed at the metal/oxide interface, indicating that the stress distribution generally follows the tetragonal phase distribution. This confirms that stress plays a crucial role in stabilising the tetragonal phase at the metal/oxide interface. The calculated uniaxial stress values at the interface reached up to 13 GPa, which corresponds approximately 4.3 GPa of hydrostatic stresses, as determined using Eq. (4). However, it is noteworthy, that the presented stress values are substantially higher than previously reported values (up to 2 GPa) [5,47]. These discrepancies may be attributed to the fact, that prior works utilised different methodologies, such as XRD, Raman point measurements, deflection, which provide average values across the volume of the oxide. In contrast, Raman imaging allows for detection of very local changes, providing information about point-specific stress rather than averaging it out. Furthermore, it is important to mention that the existing literature primarily does not focus on epitaxial stress in the oxide, which can be accurately measured using Raman imaging. It is worth emphasising that the epitaxial stress level are generally higher than stress reported during oxide growth. This helps to explain the presence of the unexpectedly high stress levels observed in our study, which, under normal circumstances, could result in material failure. However, it is important to note that these high stress levels may locally exist within specific regions.

Furthermore, for the majority of pure zirconium samples, the stress relaxation was observed while the tetragonal phase content in the oxide dropped below 10%. In addition, stress analysis through the oxide revealed a significant difference in stress distribution for the sample oxidised in water steam for 7 h, as presented in Fig. 6 (d), compared to the other samples. In the case of Zirconium oxidised in water steam for 7 h (Fig. 6 (j)), the mentioned correlation with tetragonal phase content was not observed, and the stress gradient distribution changes not uniformly. Since the highest stress value does not occur at the metal/oxide interface, where the tetragonal phase content is the highest, it is challenging to directly define all mechanisms contributing to the stabilisation of the tetragonal phase. Furthermore, it was noted that complete stress relaxation did not occur. The presence of non-uniform stress distribution, along with presence of high stress that did not gradually relax, create a detrimental situation that lead to abrupt transformations from the tetragonal to monoclinic phase. These rapid transformations throughout the entire volume of the oxide results in the formation of numerous cracks simultaneously. This likely account for the sudden

increase in oxidation rate observed in the TGA results presented in Fig. 3. Further, along with the increasing duration of the oxidation process, the stress distribution changes and begins to follow the relationship where higher tetragonal phase content corresponds to higher stress.

The comparison of the presented results after oxidation in air and water steam reveals the existence of tetragonal phase in both atmospheres. However, the role of the tetragonal phase in the corrosion resistance of zirconium oxide can be ambiguous, as it can contribute to both protective and non-protective behaviour. Generally, there is no evidence to suggest that the presence of the tetragonal phase at the interface contributes to deterioration of the oxidation resistance, as observed in the corrosion-resistant oxide formed on the zirconium surface in air. The most probable interpretation of the influence of the tetragonal phase on corrosion behaviour is that this phase can be considered protective, as long as the transformations from tetragonal to monoclinic occurs gradually. However, a dangerous situation arises when the phase transformation is largely impeded during significant oxide growth, resulting in abrupt transformations throughout the entire volume.

### 3.5. E110

Focusing on the results obtained from cross-sectional analysis of the oxide created on E110 alloy, no significant influence of the oxidation atmosphere on the tetragonal phase content and distribution was observed. The main difference was seen in oxide thickness after oxidation for 15 h in both atmospheres (Fig. 7 (b) and (e)). When comparing these results with the samples subjected to longer oxidation time (Fig. 7 (c) and (f)), it can be seen that in air, the oxide thickness decreased, while in water steam, an increase in oxide thickness was observed. This suggests that E110 exhibits better oxidation resistance in water steam than in air. Furthermore, the observed differences in both atmospheres are not as significant as in the case of pure zirconium, indicating a slighter influence of the oxidation atmosphere. Previous research on the oxidation kinetics of this alloy in air and oxygen (used to simulate water steam atmosphere) did not show differences between these atmospheres [32]. However, the presented results indicating that there may be a difference in oxidation kinetics between oxidation in air and water steam. Therefore, additional TGA measurements in water steam atmospheres could shed a new light on this area and will be included in the forthcoming paper. Despite the observed differences in oxide thickness, the thickness of the tetragonal phase remains similar. Moreover, all examined samples show a consistent correlation between stress relaxation and a decrease in tetragonal phase content with distance from the metal/oxide interface. Additionally, the carried-out analysis revealed the existence of a tetragonal phase in the bulk oxide (Fig. 7 (b)), which will be thoroughly analysed in the next section.

### 3.6. Zircaloy-2

Analysing the presented results (Fig. 8), it can be seen that regarding the examined sample, the tetragonal phase created on Zircaloy-2, after oxidation for 15 and 24 h, was significantly thinner compared to the other materials. On the other hand, SEM observations revealed a higher oxide scale thickness (Fig. 5 (c)), suggesting faster oxidation rate compared to the other materials. These results indicate a more advanced stage of the process, as the tetragonal phase fraction decreases while the oxidation continues. This observation aligns with the previous TGA measurements (Fig. 2) which presented a breakaway after 9 h. No noticeable differences in oxide thickness or tetragonal phase distribution were observed between the two employed atmospheres (Fig. 7 (c) and (f)). However, the maximal content of the tetragonal phase was significantly different. After oxidation in water steam, the tetragonal phase content was up to 50%, whereas after the same oxidation duration in air, it only reached a maximum of about 25%. This finding suggests that the

atmosphere influences oxide creation. Additionally, with an increase in oxidation duration, not only did the volume fraction of tetragonal phase decreases, but the percentage fraction also diminished. It is worth noting that all examined samples exhibited a consistent correlation between stress relaxation and decreasing tetragonal phase content with the distance from the metal/oxide interface.

### 3.7. Raman analysis of relaxed-tetragonal phase

A tetragonal phase was observed at some distance from the metal/oxide interface for the E110 sample oxidised at 600 °C for 15 h in the air. The existence of the tetragonal phase further from the metal/oxide interface (one may even suggest in bulk oxide) surrounded by a monoclinic phase was previously demonstrated in [14,48]. This phenomenon, identified as a relaxed-tetragonal phase [14,48], is correlated with tetragonal phase content, stress distribution, and full width at a high maximum (Fig. 9). The presence of this phase is accompanied by a much lower tetragonal phase content (about 10%) compared to the tetragonal phase located near the interface (up to 55%). Furthermore, both tetragonal phases are represented by different stress fields. Interface-tetragonal phase is under high compressive stress, whereas presence of the tetragonal phase in the bulk oxide is recorded despite almost complete stress relaxation (Fig. 9 (b)). Since the compressive stress observed in the bulk oxide is close to zero, it can be assumed to be relaxed, suggesting the stabilisation of interface-tetragonal and relaxed-tetragonal phases by different mechanisms. Moreover, some discrepancies can be noticed when analysing the changes in full width at high maximum parameter. At the metal/oxide interface, the FWHM of the T1 band is noticeably lower compared to the area of the relaxed-tetragonal phase (Fig. 9 (c)).

To understand better how different factors contribute to the stabilising of tetragonal phases present in different locations (at the interface and in the bulk oxide), their influence on the analysed Raman spectra needs to be elucidated. Therefore, the Raman band shift and FWHM evolution in the function of three known stabilising factors (compressive stress, grain size and stoichiometry) are presented in Table 3.

The tetragonal phase located at the metal/oxide interface is known to be stabilised by small grain size, compressive stress and high concentration of the oxygen vacancies (sub-stoichiometry) [14,19,41]. Analysed tetragonal Raman band position shifts to the higher

**Table 3**

Raman shift and FWHM changes correlation with various factors [14,19,31,41].

	Smaller grain size	Compressive stress	High concentration of oxygen vacancies
Raman shift	↑	↓	↓*
FWHM	↑	N.A.	↑

\* anticipation based on data of yttria-stabilised tetragonal phase.

frequencies with increasing distance from the interface (Fig. 9 (b)). A decrease in compressive stress accompanies this. This phenomenon suggests that compressive stress plays a more important role at the interface region than grain size, which could induce the Raman band shift in the contrary direction [41]. Changes in FWHM have been often correlated to structure disorder [14,49]. The increased value of this parameter at the interface results from the coexistence of the high concentration of oxygen vacancies and small grains size [14,25,41,49]. However, the observed change in the Raman band shift is much more significant than evolution of FWHM, suggesting once again a strong influence of stress field at the interface. This confirms, that all of these factors contribute to the stabilisation, but the impact of the compressive stresses is dominant.

Analysing the presence of the tetragonal phase in distance from the interface, marked as (1) in the Fig. 9, it can be concluded that stress does not contribute to the stabilisation of this phase, since the observed compressive stresses is very low. The difference in the FWHM parameter correlated with the structure disorder can also be identified with the inhomogeneous grain size (presence of the small grains), high concentrations of oxygen vacancies or a mix of them, which should increase with the distance from the interface [14,25,41,49]. However, in some conditions this relation can be disrupted, resulting in the existence of the relaxed tetragonal phase. Regarding the data presented in Table 3, grain size affects Raman spectra in accordance with the observed changes [41]. Nevertheless, the observed FWHM fluctuations in bulk oxide are much higher than those observed at the interface, indicating stronger influence of the stabilisation factor. The interpretation of this finding could suggest that the grain size has not increased with the distance from the interface, which contradicts the grain nucleation and growth theory [1,50].

Contrary to previous expectation, it is possible that a high

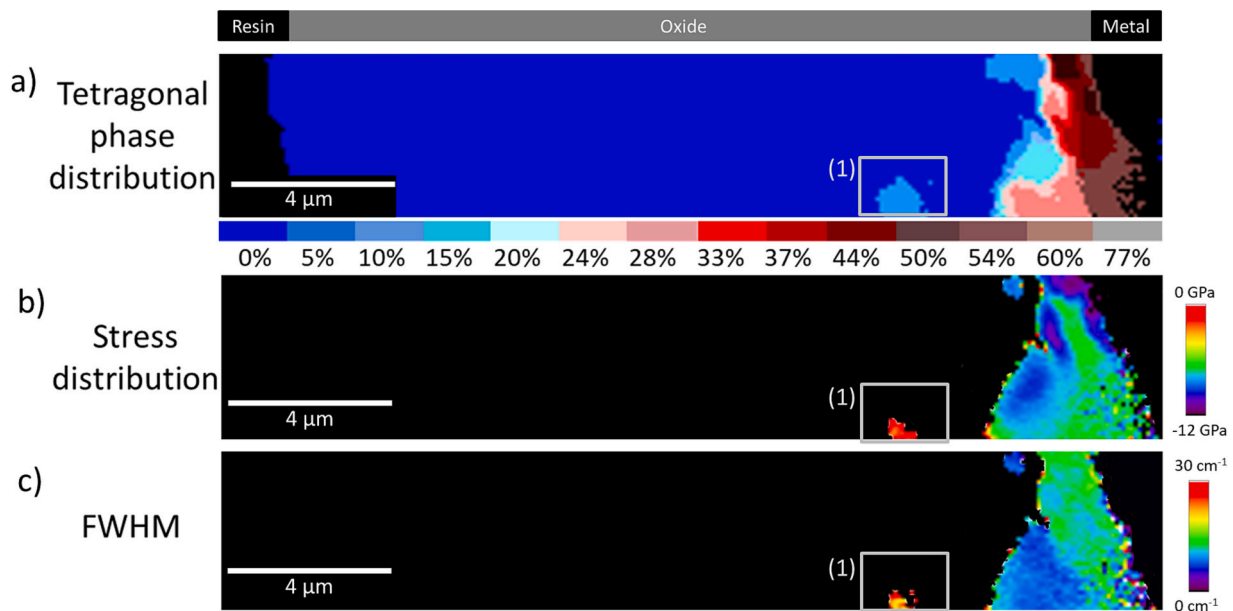


**Fig. 9.** Raman imaging results for E110 oxidised in air at 600 °C for 15 h: (a) tetragonal phase content and distribution; (b) stress distribution for T1 band; (c) distribution of full width at high maximum for T1 band; (1) marks the relaxed tetragonal phase.

concentration of oxygen vacancies can be locally created in the bulk oxide. Hence, it is suggested, that the change in high concentration of oxygen vacancies is responsible for stabilising the relaxed-tetragonal phase in this area of the oxide layer. Furthermore, the different stoichiometry than the interface tetragonal phase is evidenced by FWHM fluctuations.

The origin of the relaxed tetragonal phase remains unclear. However, at the interface, no stress relaxation with distance from the interface has been observed (similar to the behaviour of zirconium oxidised in water steam as shown in Fig. 6 (j)). Consequently, the tetragonal phase located at the interface is under high compressive stress, that are non-uniformly distributed. Assuming that the sample exhibited a high amount of the tetragonal phase distributed across the oxide a short time prior, the present circumstances suggest an abrupt transformation from the tetragonal to monoclinic phase. This observation aligns with the effect discussed in the preceding section 3.3 Pure zirconium. This phenomenon could potentially explain the rapid increase of the oxidation kinetic rate, resulting in a sudden increase in oxide thickness. The observed relaxed-tetragonal phase could then be the remnants of these transformations, that did not occurred in this particular location. Unfortunately, the question of why the transformation did not take place there remains unanswered.

#### 4. Conclusions

The objective of this study was to conduct an investigation regarding the role of the tetragonal phase in oxidation behaviour. To achieve this, various zirconium-based alloys (pure zirconium, E110, and Zircaloy-2) exposed to 600 °C for 7, 15, and 24 h, were compared. SEM and Raman imaging were used to assess their properties and tetragonal phase formation under various oxidation atmospheres. Our findings confirm and extend prior research. While numerous studies have explored this subject, our work uniquely summarizes oxidation kinetics in both air and water steam for various materials, drawing direct connections with the tetragonal phase content and stresses. Furthermore, unlike previous work that often focused on stresses in the monoclinic phase, our approach provides the stress distribution in the tetragonal phase, offering a more comprehensive view. Moreover, the implementation of Raman imaging significantly enhances the precision of the measurements.

The study's results revealed a correlation between the content and distribution of the tetragonal phase existence and stress level in all samples examined. At the metal/oxide interface, the tetragonal phase was observed to decline with increasing distance from the interface, with a similar trend observed in compressive stress level. This supports previous findings that the tetragonal phase near the metal/oxide interface is stabilised by compressive stress, and the tetragonal to monoclinic phase transformation is accompanied by stress relaxation. The abrupt change in stress level may contribute to the formation of cracks in the oxide.

Pure zirconium showed the highest sensitivity to the oxidation atmosphere among the materials examined. While it demonstrated the best oxidation resistance in air, its properties significantly deteriorated in water steam. The change in the oxidation atmosphere affected the rate of oxide growth, the distribution of the tetragonal phase, the accompanying stresses, and the ratio of tetragonal to monoclinic transformations. Although the examined materials varied in terms of tetragonal phase content, no specific correlation with oxidative behaviour was identified. This suggests that alloys have differing tendencies toward tetragonal phase formation, which does not directly influence corrosion resistance. Therefore relying solely on tetragonal phase content for comparison may lead to misinterpretations. Furthermore, within one material, the tetragonal phase content initially increases while the oxidation continues. A significant increase of tetragonal phase content in the oxide scale results in a high ratio of abrupt transformations from the tetragonal to monoclinic phase. This can be attributed to the rapid oxide

growth with a large amount of unstable tetragonal phase, requiring high compressive stresses to prevent transformations, which are difficult to sustain. Once compressive stresses become insufficient, more transformations occur, which is believed to be the cause of deteriorated corrosion resistance. Therefore, a thinner tetragonal phase observed on the examined samples (Fig. 6 (d-f) and Fig. 8 (d-f)) indicates an advanced oxidation stage. In the case of E110 and Zircaloy-2, the obtained results indicate some differences depending on the atmosphere.

A thorough analysis of oxide created on E110 revealed the presence of a tetragonal phase in the bulk monoclinic phase, commonly referred to as "relaxed tetragonal phase". The existence of this phase was determined to be accompanied by stress relaxation and structure disorder. Based on that, a differentiation of stabilisation mechanisms for the tetragonal phase was performed, depending on the existing region. Thus, the tetragonal interface phase is determined to be stabilised mainly by compressive stresses. In contrast, the relaxed tetragonal phase is stabilised by structure disorder caused by an increased number of defects, such as oxygen vacancies (indicating a changed stoichiometry).

This research presents a comprehensive investigation of the atmosphere's influence on the corrosive behaviour of various zirconium alloys, including tetragonal phase formation and accompanying effects. It lays the foundation for further studies that can provide additional insight into presented matter. The existing gap in the literature encourages the authors to conduct further studies to explain the remaining ambiguities. Especially thermogravimetric analysis carried out in water steam atmosphere will provide complete insight into the atmosphere's influence on the oxidation behaviour of different zirconium alloys. Furthermore, additional information on stress field impact on tetragonal phase stabilisation will be provided by authors using Raman measurements with high-temperature chamber and tensile stress stage.

#### Declaration of Competing Interest

The authors declare that they have no known competing financial interests or personal relationships that could have appeared to influence the work reported in this paper.

#### Data availability

The raw data required to reproduce these findings are available to download from <https://zenodo.org/communities/nomaten/>. The processed data required to reproduce these findings are available to download from <https://zenodo.org/communities/nomaten/>.

#### Acknowledgments

We acknowledge support from the European Union Horizon 2020 research and innovation program under NOMATEN Teaming grant (agreement no. 857470) and from the European Regional Development Fund via the Foundation for Polish Science International Research Agenda PLUS program grant No. MAB PLUS/2018/8.

#### References

- [1] A.T. Motta, A. Couet, R.J. Comstock, Corrosion of zirconium alloys used for nuclear fuel cladding, *Annu. Rev. Mater. Res.* 45 (April) (2015) 311–343, <https://doi.org/10.1146/annurev-matsci-070214-020951>.
- [2] P. Barberis, T. Merle-Méjean, P. Quintard, On Raman spectroscopy of zirconium oxide films, *J. Nucl. Mater.* 246 (2–3) (Aug. 1997) 232–243, [https://doi.org/10.1016/S0022-3115\(97\)00038-X](https://doi.org/10.1016/S0022-3115(97)00038-X).
- [3] L. Kurpaska, Analysis of Mechanical Stresses in Oxide Films at High Temperatures: Application to the Zr / ZrO<sub>2</sub> System, PhD thesis, UTC Compiègne, 2012.
- [4] J. Liao, et al., Critical behavior of interfacial t-ZrO<sub>2</sub> and other oxide features of zirconium alloy reaching critical transition condition, *J. Nucl. Mater.* 543 (Jan. 2021), 152474, <https://doi.org/10.1016/j.jnucmat.2020.152474>.
- [5] M. Guérain, C. Duriez, J.L. Grosseau-Poussard, M. Mermoux, Review of stress fields in Zirconium alloys corrosion scales, in: *Corrosion Science* 95, Elsevier Ltd, Jun. 01, 2015, pp. 11–21, <https://doi.org/10.1016/j.corsci.2015.03.004>.



- [6] L. Kurpaska, M. Lesniak, R. Jadach, M. Sitarz, J.J. Jasinski, J.L. Grosseau-Poussard, Shift in low-frequency vibrational spectra measured in-situ at 600 °C by Raman spectroscopy of zirconia developed on pure zirconium and Zr-1%Nb alloy, *J. Mol. Struct.* 1126 (2016) 186–191, <https://doi.org/10.1016/j.molstruc.2016.03.001>.
- [7] W. Qin, C. Nam, H.L. Li, J.A. Szpunar, Tetragonal phase stability in ZrO<sub>2</sub> film formed on zirconium alloys and its effects on corrosion resistance, *Acta Mater.* 55 (5) (Mar. 2007) 1695–1701, <https://doi.org/10.1016/j.actamat.2006.10.030>.
- [8] B.D.C. Bell, et al., The influence of alloying elements on the corrosion of Zr alloys, *Corros. Sci.* 105 (Apr. 2016) 36–43, <https://doi.org/10.1016/j.corsci.2015.12.022>.
- [9] M. Lasserre, et al., Qualitative analysis of Zircaloy-4 cladding air degradation in O<sub>2</sub>-N<sub>2</sub> mixtures at high temperature qualitative analysis of Zircaloy-4 cladding air degradation in O<sub>2</sub>-N<sub>2</sub> mixtures at high temperature, *Mater. Corros.* 65 (3) (2014), <https://doi.org/10.1002/maco.201307078i>.
- [10] P. Platt, et al., A study into stress relaxation in oxides formed on zirconium alloys, *J. Nucl. Mater.* 456 (2015) 415–425, <https://doi.org/10.1016/j.jnucmat.2014.09.072>.
- [11] J. Liao, Z. Yang, S. Qiu, Q. Peng, Z. Li, J. Zhang, The correlation between tetragonal phase and the undulated metal/oxide interface in the oxide films of zirconium alloys, *J. Nucl. Mater.* 524 (Oct. 2019) 101–110, <https://doi.org/10.1016/j.jnucmat.2019.06.039>.
- [12] I. Idarraga, M. Mermoux, C. Duriez, A. Crisci, J.P. Mardon, Potentialities of Raman imaging for the analysis of oxide scales formed on zircaloy-4 and M5® in air at high temperature, *In Oxid. Met.* 79 (3–4) (Apr. 2013) 289–302, <https://doi.org/10.1007/s11085-012-9331-5>.
- [13] M. Preuss, et al., Studies regarding corrosion mechanisms in zirconium alloys, *J. ASTM Int.* 8 (9) (2011), <https://doi.org/10.1520/JAI103246>.
- [14] C.M. Efav, et al., Characterization of zirconium oxides part I: Raman mapping and spectral feature analysis, *Nucl. Mater. Energy* 21 (Dec. 2019), 100707, <https://doi.org/10.1016/j.nme.2019.100707>.
- [15] M. Mermoux, Raman imaging in corrosion science : High-temperature oxidation of the zirconium alloys used in the nuclear industry as an example no. June (2021) 1–29, <https://doi.org/10.1002/jrs.6181>.
- [16] C.M. Efav, et al., Characterization of zirconium oxides part II: new insights on the growth of zirconia revealed through complementary high-resolution mapping techniques, *Corros. Sci.* 167 (May 2020), <https://doi.org/10.1016/j.corsci.2020.108491>.
- [17] A. Yilmazbayhan, A.T. Motta, R.J. Comstock, G.P. Sabol, B. Lai, Z. Cai, Structure of zirconium alloy oxides formed in pure water studied with synchrotron radiation and optical microscopy : relation to corrosion rate 324 (2004) 6–22, <https://doi.org/10.1016/j.jnucmat.2003.08.038>.
- [18] J. Godlewski, Oxydation d'alliages de zirconium en vapeur d'eau: influence de la zirconie tetragonale sur le me'canisme de croissance de l'oxyde, Ph.D. thesis, Univ. Technol. Compie'gne, 1990.
- [19] P. Bouvier, Ph.D. Thesis. Grenoble Inst. Technol., 2000.
- [20] L. Kurpaska, I. Jozwik, J. Jagielski, Study of sub-oxide phases at the metal-oxide interface in oxidized pure zirconium and Zr-1.0% Nb alloy by using SEM/FIB/EBSD and EDS techniques, *J. Nucl. Mater.* 476 (2016) 56–62, <https://doi.org/10.1016/j.jnucmat.2016.04.038>.
- [21] P. Barberis, Zirconia powders and Zircaloy oxide films: tetragonal phase evolution during 400°C autoclave tests, *J. Nucl. Mater.* 226 (1–2) (Oct. 1995) 34–43, [https://doi.org/10.1016/0022-3115\(95\)00108-5](https://doi.org/10.1016/0022-3115(95)00108-5).
- [22] M. Steinbrueck, F. Oliveira, M. Grosse, Oxidation of Zircaloy-4 in steam-nitrogen mixtures at 600 °C, *J. Nucl. Mater.* 490 (2017) 226–237, <https://doi.org/10.1016/j.jnucmat.2017.04.034>.
- [23] K.B. Chong, M.E. Fitzpatrick, Evolution of stress fields and phase content in corroded zirconium cladding materials, *Surf. Coat. Technol.* 324 (Sep. 2017) 140–145, <https://doi.org/10.1016/j.surfcoat.2017.05.072>.
- [24] Y. Nemoto, Y. Ishijima, K. Kondo, Y. Fujimura, Y. Kaji, Investigation of the oxidation behavior of Zircaloy-4 cladding in a mixture of air and steam, *J. Nucl. Mater.* 575 (2023), 154209, <https://doi.org/10.1016/j.jnucmat.2022.154209>.
- [25] M. Gestin, et al., Experimental study of oxidation in oxygen, nitrogen and steam mixtures at 850 °C of pre-oxidized Zircaloy-4, *J. Nucl. Mater.* 519 (Jun. 2019) 302–314, <https://doi.org/10.1016/j.jnucmat.2019.03.020>.
- [26] P. Kofstad, *High Temperature Corrosion*, 1998.
- [27] R. Hahn, *Cladding Tube Manufacturing Technology*, 1999.
- [28] C. Duriez, T. Dupont, B. Schmet, F. Enoch, Zircaloy-4 and M5 O high temperature oxidation and nitriding in air, *J. Nucl. Mater.* 380 (2008) 30–45, <https://doi.org/10.1016/j.jnucmat.2008.07.002>.
- [29] W. K. S. K. Natesan and Argonne, *Air Oxidation Kinetics for Zr-Based Alloys*, 2004.
- [30] J. Godlewski, How the Tetragonal Zirconia is Stabilized in the Oxide Scale that is Formed on a Zirconium Alloy Corroded at 400 °C in steam, in: 10th Int.Symp. Zr Nucl. Ind 1245, STP, 1994, pp. 663–686, <https://doi.org/10.3390/coatings10111057>.
- [31] P.Y. Hou, J. Ager, J. Mouglin, A. Galerie, Limitations and advantages of Raman spectroscopy for the determination of oxidation stresses, Springer (2011), <https://doi.org/10.1007/s11085-011-9235-9>.
- [32] J.L. Vandegrift, et al., Oxidation behavior of zirconium, Zircaloy-3, Zircaloy-4, Zr-1Nb, and Zr-2.5Nb in air and oxygen, *Nucl. Mater. Energy* 20 (Aug. 2019), 100692, <https://doi.org/10.1016/j.nme.2019.100692>.
- [33] K. Suchorab, L. Kurpaska, M. Gawęda, Comparison of Raman imaging assessment methods in phase determination and stress analysis of zirconium oxide layer, *Spectrochim. Acta A Mol. Biomol. Spectros.* 295 (2023) 122625, <https://doi.org/10.1016/j.saa.2023.122625>.
- [34] A.P. Naumenko, N.I. Berezovska, M.M. Biliy, O.V. Shevchenko, Vibrational analysis and Raman spectra of tetragonal zirconia, *Phys. Chem. Solid State* 9 (February 2016) (2008) 121–125.
- [35] L. Kurpaska, et al., Raman spectroscopy analysis of air grown oxide scale developed on pure zirconium substrate, *J. Nucl. Mater.* 466 (2015) 460–467, <https://doi.org/10.1016/j.jnucmat.2015.06.005>.
- [36] L. Kurpaska, M. Kozanecki, J.J. Jasinski, M. Sitarz, Stress analysis of zirconia studied by Raman spectroscopy at low temperatures, *Spectrochim. Acta - Part A Mol. Biomol. Spectrosc.* 131 (2014) 691–695, <https://doi.org/10.1016/j.saa.2014.05.023>.
- [37] L. Kurpaska, J. Favergeon, J.L. Grosseau-Poussard, L. Lahoche, G. Moulin, In-situ stress analysis of the Zr/ZrO<sub>2</sub> system as studied by Raman spectroscopy and deflection test in monofacial oxidation techniques, *Appl. Surf. Sci.* 385 (Nov. 2016) 106–112, <https://doi.org/10.1016/j.apsusc.2016.05.074>.
- [38] J. Liao, F. Xu, Q. Peng, Z. Yang, Z. Li, S. Qiu, Research on the existence and stability of interfacial tetragonal zirconia formed on zirconium alloys, *J. Nucl. Mater.* 528 (Jan. 2020), 151846, <https://doi.org/10.1016/j.jnucmat.2019.151846>.
- [39] P. Barberis, T. Merle-Méjean, P. Quintard, On Raman spectroscopy of zirconium oxide films, *J. Nucl. Mater.* 246 (2–3) (1997) 232–243, [https://doi.org/10.1016/S0022-3115\(97\)00038-X](https://doi.org/10.1016/S0022-3115(97)00038-X).
- [40] P. Bouvier, J. Godlewski, G. Lucazeau, A Raman study of the nanocrystalline size effect on the pressure-temperature phase diagram of zirconia grown by zirconium-based alloys oxidation, *J. Nucl. Mater.* 300 (2–3) (Feb. 2002) 118–126, [https://doi.org/10.1016/S0022-3115\(01\)00756-5](https://doi.org/10.1016/S0022-3115(01)00756-5).
- [41] E. Djurado, P. Bouvier, G. Lucazeau, Crystallite size effect on the tetragonal-monoclinic transition of undoped nanocrystalline zirconia studied by XRD and Raman spectrometry, *J. Solid State Chem.* 149 (2) (2000) 399–407, <https://doi.org/10.1006/JSSC.1999.8565>.
- [42] L. Kurpaska, J. Jasinski, E. Wyszowska, K. Nowakowska-Langier, M. Sitarz, Influence of Ar-ion implantation on the structural and mechanical properties of zirconia as studied by Raman spectroscopy and nanoindentation techniques, *Spectrochim. Acta - Part A Mol. Biomol. Spectrosc.* 195 (2018) 184–190, <https://doi.org/10.1016/j.saa.2018.01.074>.
- [43] T.Z. Blazynski, *Applied Elasto-Plasticity of Solids*, 1983.
- [44] A.M. Limarga, D.R. Clarke, Piezo-spectroscopic coefficients of tetragonal-prime yttria-stabilized zirconia, *J. Am. Ceram. Soc.* 90 (4) (2007) 1272–1275, <https://doi.org/10.1111/j.1551-2916.2007.01622.x>.
- [45] L.F. Kendall, R.G. Wheeler, S.H. Bush, Reaction kinetics of zirconium and Zircaloy-2 in dry air at elevated temperatures, *Nucl. Sci. Eng.* 3 (2) (1958) 171–185, <https://doi.org/10.13182/nse58-a25459>.
- [46] A.T. Motta, M.J.G. Da Silva, A. Yilmazbayhan, R.J. Comstock, Z. Cai, B. Lai, Microstructural characterization of oxides formed on model Zr alloys using synchrotron radiation, *J. ASTM Int.* 5 (3) (2008) 1–20, <https://doi.org/10.1520/JAI101257>.
- [47] N. Pétigny, P. Barberis, C. Lemaignan, C. Valot, M. Lallemand, In situ XRD analysis of the oxide layers formed by oxidation at 743 K on Zircaloy 4 and Zr-1NbO, *J. Nucl. Mater.* 280 (3) (Aug. 2000) 318–330, [https://doi.org/10.1016/S0022-3115\(00\)00051-9](https://doi.org/10.1016/S0022-3115(00)00051-9).
- [48] L. Kurpaska, J. Favergeon, L. Lahoche, G. Moulin, M. El Marssi, J.M. Roelandt, Zirconia layer formed by high temperature oxidation of pure zirconium: stress generated at the zirconium/zirconia interface, *Oxid. Met.* 79 (3–4) (2013) 261–277, <https://doi.org/10.1007/s11085-012-9348-9>.
- [49] I.L.V. Rosa, et al., Europium(III) concentration effect on the spectroscopic and photoluminescent properties of BaMoO<sub>4</sub>:Eu, *J. Fluoresc.* 19 (3) (2009) 495–500, <https://doi.org/10.1007/s10895-008-0438-7>.
- [50] G. Gottstein, *Physical foundations of materials science* 42 (05) (2005).